Modeling crystal defects using defect-informed neural networks

Ziduo Yang[1,2], Xiaoqing Liu[2], Xiuying Zhang[2], Pengru Huang[3*], Kostya S. Novoselov[3] and Lei Shen[2,4*]

[1]Department of Electronic Engineering, College of Information Science and Technology, Jinan University, Guangzhou, 510632, China.
[2]Department of Mechanical Engineering, National University of Singapore, 9 Engineering Drive 1, 117575, Singapore.
[3]Institute for Functional Intelligent Materials, National University of Singapore, 4 Science Drive 2, 117544, Singapore.
[4]National University of Singapore (Chongqing) Research Institute, Chongqing, 401123, China.

*Corresponding author(s). E-mail(s): pengru@nus.edu.sg; shenlei@nus.edu.sg;

Abstract

Machine learning has revolutionized the study of crystalline materials for enabling rapid predictions and discovery. However, most AI-for-Materials research to date has focused on ideal crystals, whereas real-world materials inevitably contain defects that play a critical role in modern functional technologies. The defects and dopants break geometric symmetry and increase interaction complexity, posing particular challenges for traditional ML models. Addressing these challenges requires models that are able to capture sparse defect-driven effects in crystals while maintaining adaptability and precision. Here, we introduce Defect-Informed Equivariant Graph Neural Network (DefiNet), a model specifically designed to accurately capture defect-related interactions and geometric configurations in point-defect structures. Trained on 14,866 defect structures, DefiNet achieves highly accurate structural predictions in a single step, avoiding the time-consuming iterative processes in modern ML relaxation models and possible error accumulation from iteration. We further validates DefiNet's accuracy by using density functional theory (DFT)

relaxation on DefiNet-predicted structures. For most defect structures, regardless of defect complexity or system size, only 3 ionic steps are required to reach the DFT-level ground state. Finally, comparisons with scanning transmission electron microscopy (STEM) images confirm DefiNet's scalability and extrapolation beyond point defects, positioning it as a groundbreaking tool for defect-focused materials research.

1 Introduction

Studying crystalline materials and their devices necessarily requires investigating defects. On one hand, defects are intrinsic and unavoidable in crystals, often significantly limiting device performance. On the other hand, defect engineering, the deliberate introduction of extrinsic defects into materials, is crucial for unlocking novel properties and functionalities in crystalline materials, enabling advancements in modern functional technologies [1–4]. For instance, point defects can introduce gap states for achieving n-type or p-type doping in semiconductors. In quantum computing, controllable point defects can serve as spin states for qubits.

The defect space is primarily defined by three variables: the host structure, the types of defects, and defect configurations [2]. The types of defects are limited to a few categories, such as intrinsic vacancies and impurity substitutions. However, the space for defect configurations is immense, making thorough experimental or computational investigations very challenging [5]. These defects typically induce local lattice distortions. To optimize the defect structures, one typically performed conventional *ab initio* methods such as density functional theory (DFT), as depicted in Fig. 1(a). DFT calculations involve iterative electronic and ionic steps that gradually converge the system to its lowest energy configuration. These steps are computationally expensive, with the time scaling approximately as N^3 where N is the number of atoms, making DFT calculations particularly challenging for large or complex systems.

The emerging technique of machine learning (ML) interatomic potentials [6–11] has shown the potential in reducing computational demands associated with defect structure optimization. By training a graph neural network (GNN) to iteratively approximate physical quantities such as energies, forces, and stresses, ML-potential relaxation bypasses the computationally intensive electronic step while retaining the ionic step, as shown in Fig. 1(b). For example, Mosquera-Lois et al. [12] and Jiang et al. [13] have demonstrated that ML interatomic potentials can provide both cost-effectiveness and accuracy in identifying the ground-state configurations of defect structures. Despite these advantages, three primary challenges remain in applying ML interatomic potentials to the study of defect structures. First, existing ML interatomic
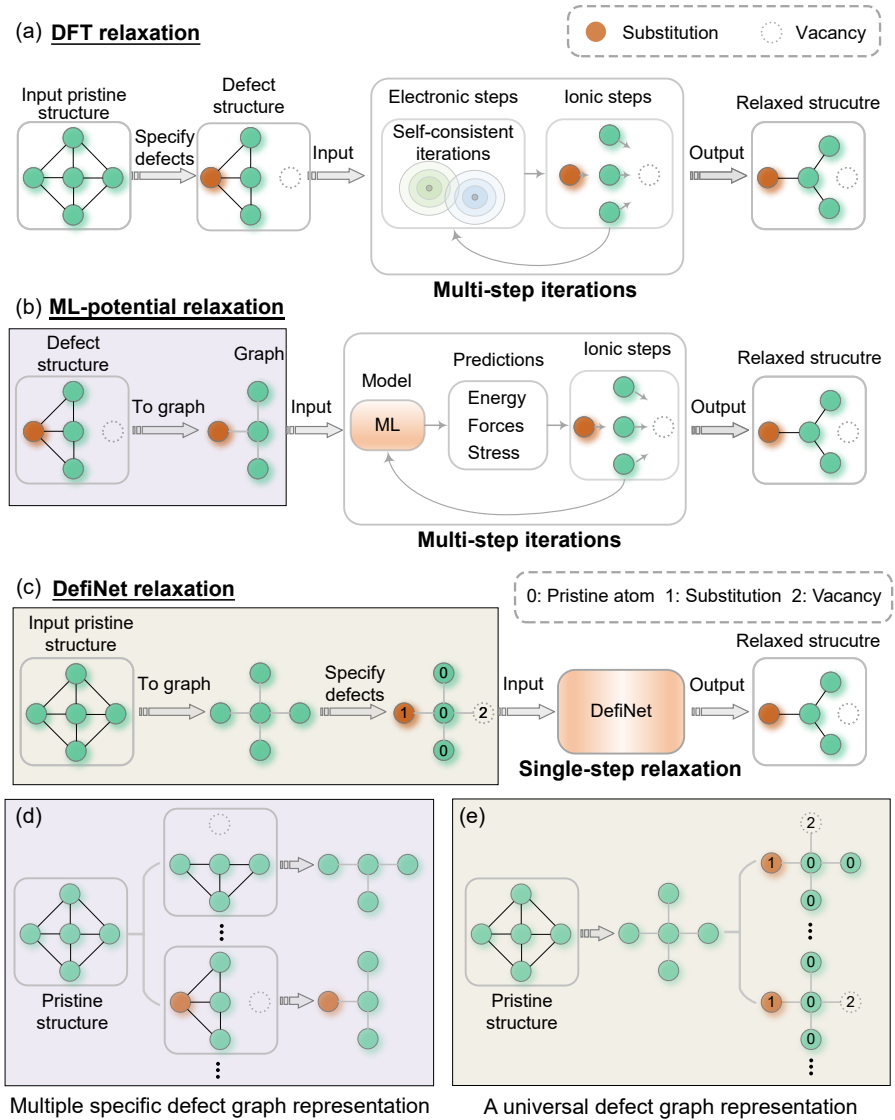
Fig. 1 Overview of crystal defect structure relaxation methods. (a) Relaxation using DFT with multi-step iterations. (b) Relaxation using ML potentials with multi-step iterations. (c) Relaxation using our DefiNet with a single step. (d) The traditional specific graph representation for defect structures. (e) Our proposed universal defect graph representation.

potentials do not explicitly consider the complicated defect-related interactions. Second, the development of ML interatomic potentials heavily relies on the availability of comprehensive databases with detailed labels for energy, forces, or stresses during structural relaxations, which may not always be available for complex defect systems. Third, ML-potential relaxation cannot

completely eliminate the iterative process, which limits its scalability and parallel computing efficiency in large-scale defect systems.

To overcome these challenges, we develop the Defect-Informed Equivariant Graph Neural Network (DefiNet), a single-step ML model specifically designed for the rapid relaxation of defect crystal structures without requiring any iterative process as shown in Fig. 1(c). DefiNet offers four key advantages:

1) Universal defect-informed representation—Traditional GNN-based representations require the reconstruction of a defect-specific graph for each new defect (Fig. 1(d)), i.e., requiring n input graphs for n defect structures, much like how DFT calculations require a unique input for each defect configuration. In contrast, DefiNet employs a single graph constructed from the host structure, augmented with markers to represent defects (referred to as a universal defect graph representation), as shown in Fig. 1(e). To explicitly capture complex defect-related interactions, we introduce defect-aware message passing on the universal defect graph, resulting in a more accurate representation of defect structures.

2) End-to-end trainability—DefiNet directly maps initial structures to relaxed configurations, enabling efficient end-to-end training and scalable parallel computing capabilities. This makes it highly suitable for large-scale calculations as it completely eliminates iterative relaxation steps.

3) Equivariant representation—The model leverages equivariant representation to ensure that rotational transformations of the input structure are consistently reflected throughout the network's layers and in the final output coordinates, leading to more precise geometric representations.

4) Scalability—It is well known that in conventional DFT or ML interatomic potential approaches, computational cost increases significantly with structural complexity and the total number of atoms due to their reliance on iterative algorithms. In contrast, DefiNet's single-step and end-to-end design enable it to accurately predict defect structures regardless of defect complexity or system size.

We evaluated DefiNet on 14,866 defect structures across six widely studied materials, including MoS_2, WSe_2, h-BN, GaSe, InSe, and black phosphorus (BP), each presenting a variety of defects. Our results show that with just a few hundred training samples per material, DefiNet achieves precise structural relaxation within tens of milliseconds using a single GPU, even without utilizing its parallel computing capabilities. To validate the accuracy and efficiency, we use the original unrelaxed structures and DefiNet-predicted structures as initial configurations for DFT calculations. DefiNet improves the computational efficiency by 87%, demonstrating DefiNet's efficiency in identifying energetically favorable configurations. Moreover, DefiNet efficiently scales from small to large systems while maintaining its ability to generalize between high- and low-defect-density scenarios. Comparisons with high-resolution scanning transmission electron microscopy (STEM) images of complex defects, such as

line defects, further validate the model's scalability and extrapolation capabilities beyond point defects. Collectively, these advancements establish DefiNet as a powerful tool for defect-focused materials and device research.

2 Methods

2.1 Input representation

In this work, the defect structure is represented as a universal defect graph $\mathcal{G} = (\mathcal{V}, \mathcal{E}, \mathcal{M})$, where $\mathcal{V}$ and $\mathcal{E}$ are sets of nodes and edges corresponding to atoms and bonds within the pristine structure, and $\mathcal{M}$ is a set of markers representing defect types. Each marker $m_i \in \mathcal{M}$ is a categorical variable that takes a value from the set $\{0, 1, 2\}$, where 0 denotes a pristine atom, 1 indicates a substitution, and 2 represents a vacancy. Each node $v_i \in \mathcal{V}$ contains three feature types: scalar $\boldsymbol{x}_i \in \mathbb{R}^F$, vector $\vec{\boldsymbol{x}}_i \in \mathbb{R}^{F \times 3}$, and coordinates $\vec{r}_i \in \mathbb{R}^3$, which encapsulate invariant, equivariant, and structural features, respectively. The number of features F is kept constant throughout the network. The scalar feature is initialized as an embedding dependent solely on the atomic number, given by $\boldsymbol{x}_i^{(0)} = E(z_i) \in \mathbb{R}^F$, where z_i is the atomic number and E is an embedding layer that takes z_i as input and returns an F-dimensional feature. The vector feature is initially set to $\vec{\boldsymbol{x}}_i^{(0)} = \vec{\mathbf{0}} \in \mathbb{R}^{F \times 3}$. To capture long-range interactions, we introduce a virtual node $v_{\mathcal{G}}$, which includes a virtual scalar $\boldsymbol{x}_{\mathcal{G}} \in \mathbb{R}^F$ and a virtual vector $\vec{\boldsymbol{x}}_{\mathcal{G}} \in \mathbb{R}^{F \times 3}$. These are initialized as a trainable F-dimensional feature and $\vec{\mathbf{0}}$, respectively. We also define the relative position vector as $\vec{r}_{ij} = \vec{r}_j - \vec{r}_i$. Each node is connected to its closest neighbors within a cutoff distance D, with a maximum number of neighbors N, where D and N are predefined constants. Given a set of universal defect graphs, our goal is to learn a model f that directly maps initial defect structures to their final relaxed configurations.

2.2 DefiNet workflow

The proposed DefiNet consists of four layers, each of which updates the node representation through a three-stage graph convolution process that includes defect-aware message passing, self-updating, and defect-aware coordinate updating. This process incorporates message distribution and aggregation to capture long-range interactions, as illustrated in Fig. 2. First, message distribution propagates information globally from the virtual node $v_{\mathcal{G}}$ to each node v_i. Second, defect-aware message passing is applied locally to collect messages from neighboring nodes v_j for a node v_i, mimicking atomic two-body interactions. Third, a self-updating phase refines the information within each node. Fourth, defect-aware coordinate updating is utilized to refine the atomic coordinates, optimizing the structure. Finally, message aggregation collects information from all nodes globally to update the virtual node. The message

distribution and aggregation promote information exchange between the virtual node and other nodes, thereby enhancing the model's ability to capture long-range interactions.
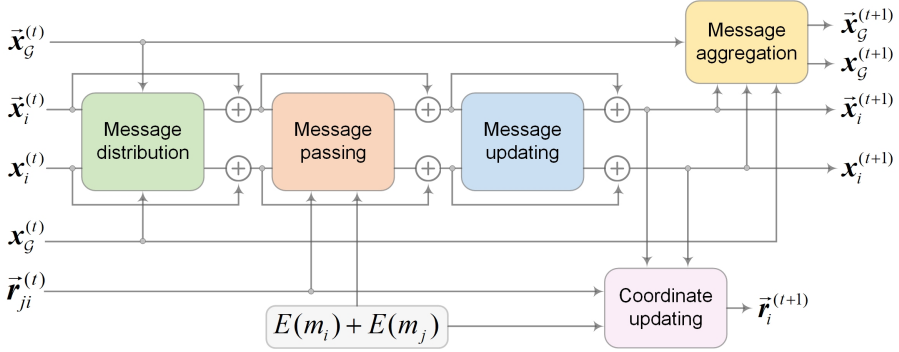

Fig. 2 Workflow of the t-th graph convolution layer in DefiNet. The process begins with message distribution, where the virtual scalar $x_{\mathcal{G}}^{(t)}$ and virtual vector $\vec{x}_{\mathcal{G}}^{(t)}$ are globally distributed to each scalar $x_i^{(t)}$ and vector $\vec{x}_i^{(t)}$. This is followed by message passing, which locally collects messages from neighboring nodes v_j, incorporating the relative position vector $\vec{r}_{ji}^{(t)}$ to capture geometric relationships between atoms, while also considering defect types m_i and m_j. Next, message updating refines the node representation using the information within the node itself, resulting in $x_i^{(t+1)}$ and $\vec{x}_i^{(t+1)}$. Coordinate updating then further refines the atomic coordinates, resulting in the updated coordinates $\vec{r}_i^{(t+1)}$. Finally, message aggregation is performed to update the global scalar and vector, resulting in $x_{\mathcal{G}}^{(t+1)}$ and $\vec{x}_{\mathcal{G}}^{(t+1)}$.

2.3 Defect-aware message passing

In the t-th layer, during defect-aware message passing, a node v_i gathers messages from its neighboring nodes v_j, including scalars $x_j^{(t)}$ and vectors $\vec{x}_j^{(t)}$, while taking defect types into consideration. This process results in intermediate scalar and vector variables q_i and $\vec{q}_i$, defined as follows:

$$q_i = \sum_{v_j \in \mathcal{N}(v_i)} (W_h x_j^{(t)}) \circ \lambda_h(\|\vec{r}_{ji}^{(t)}\|) \circ \gamma_h\big(E(m_i) + E(m_j)\big) \tag{1}$$

$$\vec{q}_i = \sum_{v_j \in \mathcal{N}(v_i)} (W_u x_j^{(t)}) \circ \lambda_u(\|\vec{r}_{ji}^{(t)}\|) \circ \gamma_u\big(E(m_i) + E(m_j)\big) \circ \vec{x}_j^{(t)}$$
$$+ (W_v x_j^{(t)}) \circ \lambda_v(\|\vec{r}_{ji}^{(t)}\|) \circ \gamma_v\big(E(m_i) + E(m_j)\big) \circ \frac{\vec{r}_{ji}^{(t)}}{\|\vec{r}_{ji}^{(t)}\|} \tag{2}$$

Here, E is an embedding layer convert the marker m_i to an F-dimensional feature, and γ_h, γ_u, and γ_v are multilayer perceptron (MLP), The matrices $\boldsymbol{W}_h, \boldsymbol{W}_u, \boldsymbol{W}_v \in \mathbb{R}^{F \times F}$ are learnable. The functions λ_h, λ_u, and λ_v are the linear combination of Gaussian radial basis functions [14].

2.4 Self-updating

We employ the self-updating mechanism proposed by Yang et al. [15]. During this phase, the F scalars and F vectors within $\boldsymbol{q}_i$ and $\vec{\boldsymbol{q}}_i$, respectively, are aggregated to generate the updated scalar $\boldsymbol{x}_i^{(t+1)}$ and vector $\vec{\boldsymbol{x}}_i^{(t+1)}$. Specifically, the scalar representation $\boldsymbol{x}_i^{(t+1)}$ and vector representation $\vec{\boldsymbol{x}}_i^{(t+1)}$ are updated according to the following equations:

$$\boldsymbol{x}_i^{(t+1)} = \boldsymbol{W}_s\big(\boldsymbol{q}_i \oplus \|\boldsymbol{V}\vec{\boldsymbol{q}}_i\|\big) + \tanh\big(\boldsymbol{W}_g\big(\boldsymbol{q}_i \oplus \|\boldsymbol{V}\vec{\boldsymbol{q}}_i\|\big)\big)\boldsymbol{q}_i \tag{3}$$

$$\vec{\boldsymbol{x}}_i^{(t+1)} = \boldsymbol{W}_h\big(\boldsymbol{q}_i \oplus \|\boldsymbol{V}\vec{\boldsymbol{q}}_i\|\big) \circ \boldsymbol{U}\vec{\boldsymbol{q}}_i \tag{4}$$

where $\oplus$ denotes concatenation, $\boldsymbol{W}_s, \boldsymbol{W}_g, \boldsymbol{W}_h \in \mathbb{R}^{F \times 2F}$, and $\boldsymbol{U}, \boldsymbol{V} \in \mathbb{R}^{F \times F}$.

2.5 Defect-aware coordinate updating

The defect-aware coordinate updating step aims to refine the atomic coordinates using two modules, RPV2ΔCoord and Vec2ΔCoord, which represent two distinct contributions to the coordinate update. Specifically, RPV2ΔCoord converts the relative position vector $\vec{\boldsymbol{r}}_{ji}^{(t)}$ into a delta coordinate, while Vec2ΔCoord translates the vector representation $\vec{\boldsymbol{x}}_i^{(t+1)}$ into a delta coordinate. Together, these determine the movement direction of each atom at the current stage, as described by the following equations:

$$\Delta_r^{\text{RPV}} = \boldsymbol{W}_p\vec{\boldsymbol{x}}_i^{(t+1)} \tag{5}$$

$$\Delta_r^{\text{Vec}} = \boldsymbol{W}_q\Big(\big(\boldsymbol{W}_v\boldsymbol{x}_j^{(t+1)}\big) \circ \lambda_v\big(\|\vec{\boldsymbol{r}}_{ji}^{(t)}\|\big) \circ \gamma_v\big(E(m_i) + E(m_j)\big)\Big) \circ \frac{\vec{\boldsymbol{r}}_{ji}^{(t)}}{\|\vec{\boldsymbol{r}}_{ji}^{(t)}\|} \tag{6}$$

where $\boldsymbol{W}_p \in \mathbb{R}^{1 \times F}$ integrates all the vectors within $\vec{\boldsymbol{x}}_i^{(t+1)}$, and $\boldsymbol{W}_q \in \mathbb{R}^{1 \times F}$ projects the F-dimensional features into scalar values. Finally, the coordinates are updated as follows:

$$\vec{\boldsymbol{r}}_i^{(t+1)} = \vec{\boldsymbol{r}}_i^{(t)} + \Delta_r^{\text{RPV}} + \Delta_r^{\text{Vec}} \tag{7}$$

The initial coordinate $\vec{\boldsymbol{r}}_i^{(0)}$ is set to the atom coordinate of the unrelaxed structure.

2.6 Message distribution and aggregation

To establish a more effective global communication channel across the entire graph, we implement a message distribution and aggregation scheme using virtual node technology [15]. The message distribution process propagates the global scalar and vector at the current step to each node using the following equations:

$$\boldsymbol{x}_i^{(t)} = \phi(\boldsymbol{x}_i^{(t-1)} \oplus \boldsymbol{x}_\mathcal{G}^{(t-1)}) + \boldsymbol{x}_i^{(t-1)} \tag{8}$$

$$\vec{\boldsymbol{x}}_i^{(t)} = \boldsymbol{W}(\vec{\boldsymbol{x}}_i^{(t-1)} + \vec{\boldsymbol{x}}_\mathcal{G}^{(t-1)}) + \vec{\boldsymbol{x}}_i^{(t-1)} \tag{9}$$

where $\phi : \mathbb{R}^{2F} \to \mathbb{R}^F$ is an MLP, and $\boldsymbol{W} \in \mathbb{R}^{F \times F}$ is a trainable matrix.

The message aggregation step updates the global scalar and vector based on the node representations at the current step, as described by the following equations:

$$\boldsymbol{x}_\mathcal{G}^{(t+1)} = \phi\left(\left(\frac{1}{|\mathcal{G}|}\sum_{v_i \in \mathcal{G}} \boldsymbol{x}_i^{(t)}\right) \oplus \boldsymbol{x}_\mathcal{G}^{(t)}\right) + \boldsymbol{x}_\mathcal{G}^{(t)} \tag{10}$$

$$\vec{\boldsymbol{x}}_\mathcal{G}^{(t+1)} = \boldsymbol{W}\left(\left(\frac{1}{|\mathcal{G}|}\sum_{v_i \in \mathcal{G}} \vec{\boldsymbol{x}}_i^{(t)}\right) + \vec{\boldsymbol{x}}_\mathcal{G}^{(t)}\right) + \vec{\boldsymbol{x}}_\mathcal{G}^{(t)} \tag{11}$$

2.7 Non-linear vector activation

Non-linearity is essential for enhancing the expressive power of neural networks. Here, we introduce non-linearity into vector representations while preserving equivariance. Specifically, we first aggregate the F vectors within a node to obtain a global vector for each node:

$$\vec{\boldsymbol{x}}_i^\mathcal{G} = \boldsymbol{W}_p \vec{\boldsymbol{x}}_i \tag{12}$$

where $\boldsymbol{W}_p \in \mathbb{R}^{1 \times F}$ integrates all vectors within $\vec{\boldsymbol{x}}_i$ to produce the global vector $\vec{\boldsymbol{x}}_i^\mathcal{G} \in \mathbb{R}^3$, capturing the overarching trend across all vectors in the node. Next, each vector $\vec{\boldsymbol{x}}_i^j$ within $\vec{\boldsymbol{x}}_i$ is updated as follows:

$$\vec{\boldsymbol{x}}_i^j = \begin{cases} \boldsymbol{W}^j \vec{\boldsymbol{x}}_i, & \text{if } \langle \vec{\boldsymbol{x}}_i^\mathcal{G}, \boldsymbol{W}^j \vec{\boldsymbol{x}}_i \rangle > 0 \\ \boldsymbol{W}^j \vec{\boldsymbol{x}}_i + \vec{\boldsymbol{x}}_i^\mathcal{G}, & \text{otherwise} \end{cases} \tag{13}$$

Here, $\boldsymbol{W}^j \in \mathbb{R}^{1 \times F}$, and $\langle \cdot, \cdot \rangle$ denotes the dot product. The idea is that if the vectors align with the global trend, as indicated by a dot product greater than zero, they are considered significant and retained without modification. Conversely, if the vectors diverge from the global trend (dot product less than or equal to zero), they are adjusted by adding the global vector, thus reorienting them closer to the global directional trend. Every time the vectors have been updated, we apply a non-linear vector activation to them.

2.8 Implementation details

The DefiNet model is implemented using PyTorch, and experiments are conducted on an NVIDIA RTX A6000 with 48 GB of memory. The training objective is to minimize the mean absolute error (MAE) loss between the ML-relaxed and DFT-relaxed structures, defined as follows:

$$\mathcal{L} = \frac{1}{N} \frac{1}{M} \sum_{i=1}^{M} \left| \boldsymbol{\bar{r}}_i^{(T)} - \boldsymbol{\tilde{r}}_i \right| \tag{14}$$

where N and M denote the sample size and the number of atoms in each sample, respectively. Here, T represents the total number of layers in the model, and $\boldsymbol{\tilde{r}}_i$ is the DFT-relaxed atomic coordinate. We use the AdamW optimizer with a learning rate of 0.0001 to update the model's parameters. Additionally, a learning rate decay strategy is implemented, reducing the learning rate if there is no improvement in coordinate MAE for 5 consecutive epochs.

2.9 DFT calculations

Our calculations are performed using density functional theory (DFT) with the Perdew-Burke-Ernzerhof (PBE) exchange-correlation functional, as implemented in the Vienna Ab Initio Simulation Package (VASP) [16]. The interaction between valence electrons and ionic cores is treated using the projector augmented wave (PAW) method [17], with a plane-wave energy cutoff of 500 eV. Initial crystal structures were taken from the Materials Project database, and details on supercell sizes for each material are provided in Table 1. Given the large supercells required for defect calculations, structural relaxations were carried out using a Γ-point only Monkhorst-Pack grid. To prevent interactions between neighboring layers, a vacuum space of at least 15 Å was introduced. During structural relaxation, atomic positions were optimized until the forces on all atoms were below 0.01 eV/Å, with an energy tolerance of 10^{-6} eV. For defect structures with unpaired electrons, we used standard collinear spin-polarized calculations, initializing magnetic ions in a high-spin ferromagnetic state, with the possibility of relaxation to a low-spin state during the ionic and electronic relaxation processes.

3 Results

3.1 DefiNet architecture

A crystal structure is typically represented as a graph $\mathcal{G} = (\mathcal{V}, \mathcal{E})$, where nodes $v_i \in \mathcal{V}$ represent atoms, and edges $e_{ij} \in \mathcal{E}$ denote the bonds between them. Since this traditional representation neglects defect information, we propose a universal defect representation approach that utilizes a single graph constructed from the host structure, augmented with markers to indicate defects, as shown in Fig. 1(e). This method offers two primary advantages. Firstly,
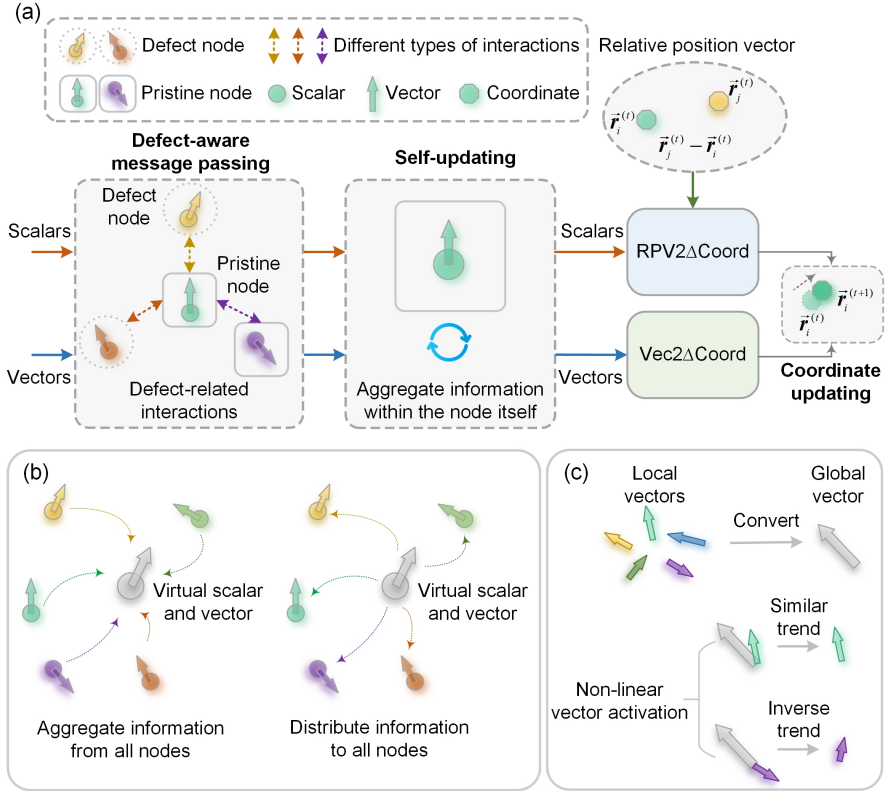
Fig. 3 Detailed designs of DefiNet. (a) Overview of the three-stage updating process, including defect-aware message passing, self-updating, and defect-aware coordinate updating. (b) Implementation of virtual scalars and vectors. (c) Non-linear vector activation technique.

it incorporates a vacancy node to represent vacancies, thereby enabling the model to capture various types of interactions, such as those between vacancies and substitutions, as well as between vacancies and pristine atoms, through our proposed defect-aware message passing mechanism in DefiNet. Secondly, it eliminates the need to construct multiple defect-specific graphs, significantly streamlining the process.

DefiNet is a graph neural network (GNN) [6–8, 14, 18–36] specifically designed to capture complex defect-related interactions and analyze the geometric configurations of defect structures. The overall architecture of DefiNet is depicted in Fig. 3(a). The model employs a vector-scalar-coordinate triplet representation to encapsulate invariant, equivariant, and structural features, respectively. Scalar features $\boldsymbol{x}_i \in \mathbb{R}^F$ for node v_i encode information related to the material's properties that are invariant to geometric transformations. Vector features $\vec{\boldsymbol{x}}_i \in \mathbb{R}^{F \times 3}$ provide geometrical information that is equivariant to rotations. The initial coordinates, $\vec{r}_i \in \mathbb{R}^3$, are updated through successive layers to optimize the structure toward a more stable state.

DefiNet updates this triplet representation through a three-stage graph convolution process as illustrated in Fig. 3(a). The process begins with defect-aware message passing, which aggregates information from neighboring nodes to simulate atomic interactions, while also considering various interaction types, including those among defects, between defects and pristine atoms, and among pristine atoms themselves. This message passing mechanism aligns with the nearsightedness principle [37], which posits that local electronic properties depend primarily on nearby changes in potential, while distant perturbations have diminishing influence. The self-updating stage then updates the scalar and vector features using the node's internal information. The final stage, defect-aware coordinate updating, optimizes atom coordinates using two specific modules, namely the Relative Position Vector to Delta Coordinate (RPV2ΔCoord) and Vector to Delta Coordinate (Vec2ΔCoord). These modules calculate "delta coordinates", which represent the necessary displacements to move each atom toward an optimized structure.

DefiNet further incorporates two technologies to boost model performance. First, drawing inspiration from the virtual node strategy [38, 39], we introduce virtual scalar and vector components to capture long-range interactions, as illustrated in Fig. 3(b). These virtual components aggregate scalar and vector information from all nodes across the graph and subsequently redistribute it to each node, thereby enhancing the model's ability to identify long-range interactions effectively. Second, while non-linearity is crucial for the expressive power of neural networks, introducing non-linearity into vector representations without compromising equivariance presents a challenge [40]. To address this, we have introduced a novel nonlinear vector activation, as illustrated in Fig. 3(c). This method employs a global vector to capture the overarching trend across all vectors. Vectors that align with this global trend, as indicated by a dot product greater than zero, are deemed significant and retained without changes. In contrast, vectors that diverge from this trend, shown by a dot product less than zero, are modified by adding the global vector, thus reorienting them closer to the global directional trend.

3.2 Database

We have developed a database for 2D material defects (2DMD) [2, 4], to facilitate the training and evaluation of ML models for defect structure analysis. This database includes structures with point defects for commonly used 2D materials including MoS_2, WSe_2, h-BN, GaSe, InSe, and black phosphorous (BP). Details of these point defects with supercell specifications are presented in Table 1.

The database is divided into two sections: one with a low-density of structured defect configurations, and another with a high-density of randomly configured defects. The low-density section includes 5,933 structures each for MoS_2 and WSe_2, with 1 to 3 defects per structure, covering all potential configurations within an 8×8 supercell. The high-density section comprises randomly generated substitution and vacancy defects across all six materials. For each

Table 1 Overview of point defect types and DFT calculation parameters for the 2DMD datasets

Materials	Substitutions	Vacancies	Supercell	Cell size (Å)
MoS_2	S → Se; Mo → W	Mo; S	8×8	(25.52, 25.52, 20)
WSe_2	Se → S; W → Mo	W; Se	8×8	(26.62, 26.62, 20)
h-BN	B → C; N → C	B; N	8×8	(20.10, 20.10, 20)
GaSe	Ga → In; Se → S	Ga; Se	6×6	(22.91, 22.91, 20)
InSe	In → Ga; Se → S	In; Se	6×6	(24.58, 24.58, 20)
BP	P → N	P	6×6	(19.80, 27.61, 20)

defect concentration—2.5%, 5%, 7.5%, 10%, and 12.5%—100 structures were created, resulting in a total of 500 configurations per material and 3,000 overall. In total, the dataset contains 14,866 structures, each comprising 120–192 atoms after applying supercell expansion.

The datasets are stratified and split into training, validation, and test sets in a ratio of 8:1:1. The validation set is used to monitor model performance and select the best-performing model for further evaluation on the test set.

3.3 Evaluation Metric

We use the coordinate MAE between the ML-relaxed and DFT-relaxed structures to evaluate the model's performance. Since structural variations between unrelaxed and relaxed defect structures are primarily localized near the defect sites, we further introduce localized MAE statistics for a more precise assessment of model's performance. Specifically, we denote atoms within an x Å radius of the defect sites as A_x, where x is set to 3, 4, 5, and 6 in our experiments. For example, the coordinate MAE for A_5 considers only atoms within a 5 Å radius of the defect site when calculating the MAE.

3.4 Model performance on structures with low-density defects

We first benchmark DefiNet on structures with low-density defects, comparing it against the state-of-the-art (SOTA) single-step ML model, DeepRelax [41]. As a baseline, we introduce a Dummy model that simply returns the input initial structure as its output, serving as a control reference for evaluation. All models are trained, validated, and tested on identical datasets.

Fig. 4(a)-(b) presents the performance of the models, showing that both DeepRelax and DefiNet significantly outperform the Dummy model. DefiNet surpasses DeepRelax notably, achieving improvements of 78.38%, 61.86%, 64.77%, 66.67%, and 70.37% in coordinate MAE for all atoms, A_3, A_4, A_5, and A_6, respectively, across all defect structures in both materials. Additionally, DefiNet is approximately 26.2 times more computationally efficient than DeepRelax, as shown in Suppl. Table 1.
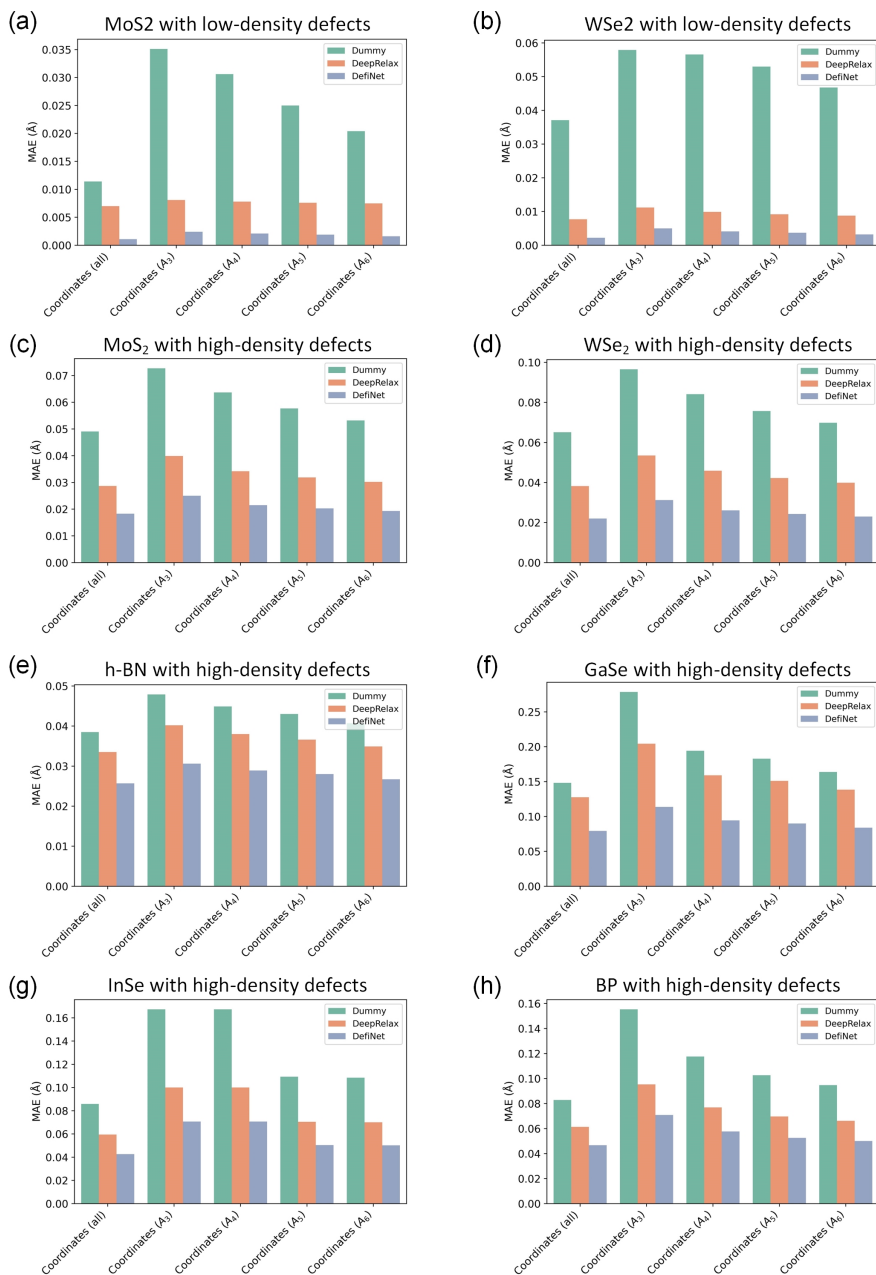
Fig. 4 Model performance for structures with low- and high-density defects. (a) MoS_2 and (b) WSe_2 with low-density defects, and (c) MoS_2, (d) WSe_2, (e) h-BN, (f) GaSe, (g) InSe, and (h) BP with high-density defects. A_3, A_4, A_5, and A_6 represent MAE calculations using only atoms within 3Å, 4Å, 5Å, and 6Å radii around defect sites, respectively.

3.5 Model performance on structures with high-density defects

While low-density defects are more commonly studied, they represent only a small portion of the entire defect space. High-density defects can reveal important and unique physical phenomena that low-density studies may not capture. In particular, interactions between multiple defects can significantly influence material properties in ways that isolated defects cannot. These complex defect-related interactions pose a significant challenge for ML models.

Here, we demonstrate that DefiNet also achieves strong performance on structures with high-density defects, as shown in Fig. 4(c)-(h). We make three key observations: First, DefiNet proves to be robust across multiple materials. Second, compared to the results in Fig. 4(a)-(b), both DeepRelax and DefiNet show less significant improvements, likely due to the smaller sample size in the high-density defect datasets and the more complex defect-related interactions. Third, DefiNet still significantly outperforms DeepRelax, with improvements of 32.82%, 35.88%, 34.08%, 33.88%, and 33.33% in coordinate MAE for all atoms, A_3, A_4, A_5, and A_6 respectively, across all defect structures in the six materials.

3.6 DFT validation

Validating the energetic favorability of ML-predicted structures is essential to ensuring their physical relevance, accuracy, and efficiency. While coordinate errors provide insight into geometrical accuracy, further analysis is needed to confirm that the predicted structures correspond to local minima on the potential energy surface. We conducted DFT validations to assess whether the structures relaxed by DefiNet are the same as or very similar to DFT ones. For this, we randomly selected 25 WSe_2 and 25 MoS_2 low-density defect structures for DFT validations. Detailed settings for the DFT calculations are provided in subsection 2.9.

We compared the number of ionic steps required for convergence in two cases: starting from unrelaxed structures and starting from DefiNet-predicted structures. The results, shown in Fig. 5(a), indicate that using DefiNet-predicted structures as starting points significantly reduces the computational effort required for DFT relaxation, with the number of ionic steps decreasing by approximately 87%. Notably, these residual ionic steps also remain nearly constant, regardless of defect complexity. The very low residual ionic steps demonstrate the high accuracy of DefiNet. The steady residual ionic steps, even for highly complex defects, highlight the exceptional efficiency of DefiNet. Additional DFT validation results for high-density defect scenarios are available in Suppl. Fig. 1, which also demonstrates DefiNet's promising performance.

To evaluate the scalability of DefiNet, we tested its performance across different supercell sizes. Specifically, we randomly selected five defect structures
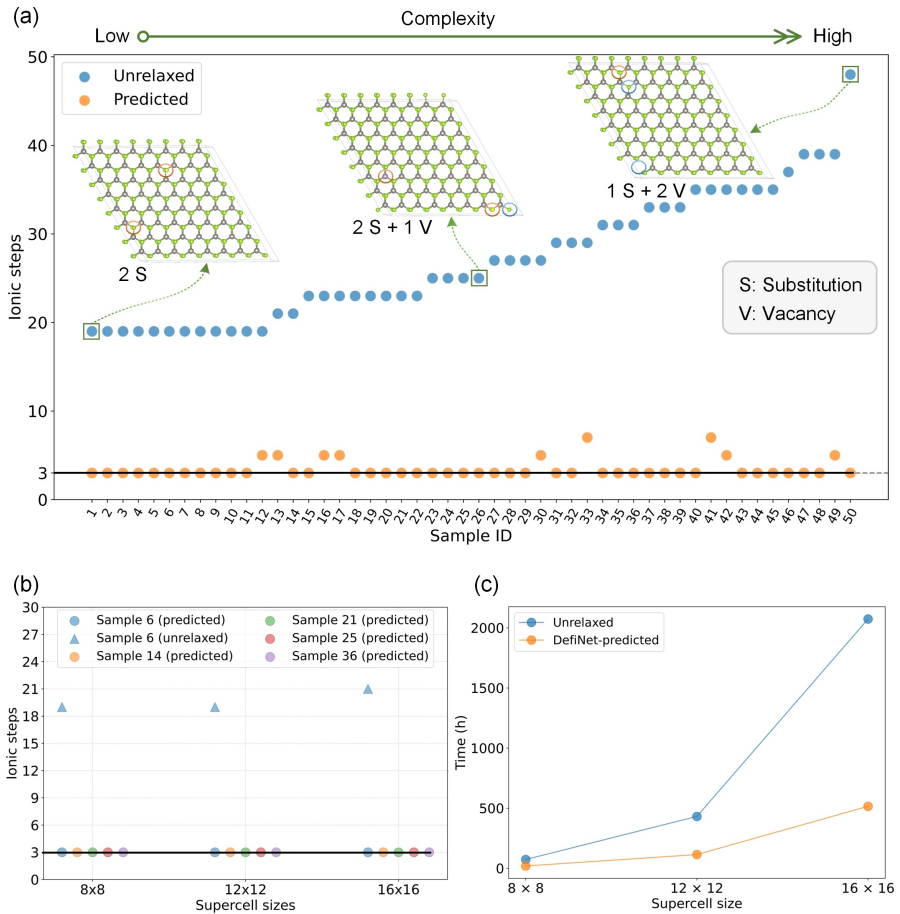
Fig. 5 DFT validation on DefiNet's accuracy, efficiency, and scalability. (a) Comparison of the number of DFT ionic steps required to relax structures starting from the initial unrelaxed configurations and from the DefiNet-predicted structures for low-density defects. The steady residual ionic steps against the **defect complexity** are indicated by a horizontal black solid line. The sample ID is sorted based on the number of ionic steps required by the unrelaxed structures for better observation. (b) Residual ionic steps for five randomly selected defect structures from the 50 samples across different supercell sizes, starting from both unrelaxed and DefiNet-predicted configurations. The steady residual ionic steps against the **structural size** are indicated by a horizontal black solid line. (c) Comparison of DFT CPU core hours on large supercells using unrelaxed and DefiNet-predicted configurations.

from the test set containing different types of defects. We then created supercells with sizes of 8×8, 12×12, and 16×16, resulting in structures with around 190 atoms, 430 atoms, and 770 atoms, respectively. DefiNet was used to predict the relaxed structures for these unrelaxed configurations. We assessed both the residual ionic steps and the CPU core hours required for the DefiNet-predicted structures, comparing these results to those of the unrelaxed structures.

As illustrated in Fig. 5(b), DefiNet consistently achieves constant ionic steps of 3, irrespective of the system size, demonstrating its ability to scale effectively with increasing system size. We further compare the CPU core hours required for the relaxation of both unrelaxed and DefiNet-predicted structures. Due to the extremely high computational cost associated with the unrelaxed structure of the 16×16 supercell size with 770 atoms, only one sample was selected as an example for this experiment. As shown in Fig. 5(c), the computational cost for the large-scale unrelaxed structure is extremely high. In contrast, the relaxation time for the DefiNet-predicted structures is significantly reduced, highlighting DefiNet's capability for large systems by dramatically decreasing the computational cost. Further scalability evaluations are detailed in Suppl. Note 3.

3.7 Visualization and experimental validation

Fig. 6(a) illustrates the detailed local distortions by comparing unrelaxed, DFT-relaxed, and DefiNet-predicted structures. As can be seen, the DefiNet-predicted structure closely matches the DFT-relaxed structure, demonstrating the model's effectiveness in handling complex defect configurations. To further validate the accuracy and extrapolation of DefiNet using experimental results, we conducted comparisons with STEM images, assessing the alignment between DefiNet-relaxed structures and actual experimental observations. Fig. 6(b)-(d) shows STEM images (overlaid with the DefiNet-relaxed structure) of MoS_2 [42] and WSe2 [43] with different types of complex defects, including in line defects, mixed single Se (SV_{Se}) with double Se vacancies (DV_{Se}), and a three-fold symmetric trefoil defect. The strong alignment between the DefiNet-predicted and experimentally observed structures highlights DefiNet's accuracy and extrapolation in capturing such complex defects beyond the training point defects.

3.8 Comparison to ML-potential relaxation

ML-potential relaxation is a popular alternative to DFT-based relaxation methods. To demonstrate the superiority of DefiNet, we compare it against two well-known ML-potential models: M3GNet and CHGNet. These methods typically require large datasets to train GNN surrogate models that iteratively approximate physical quantities such as energies, forces, and stresses. For this comparison, we used the MoS_2 low-density defect dataset, which contains a sufficient number of samples (5,933) with detailed information obtained during DFT-based relaxation. All methods were trained, validated, and tested on the same data splits. Detailed experimental settings are provided in Suppl. Note 4. As shown in Suppl. Fig. 4, DefiNet significantly outperforms M3GNet, CHGNet, and DeepRelax in terms of coordinate MAE and robustness. This result is further validated by DFT calculations, with detailed comparisons available in Suppl. Fig. 5.
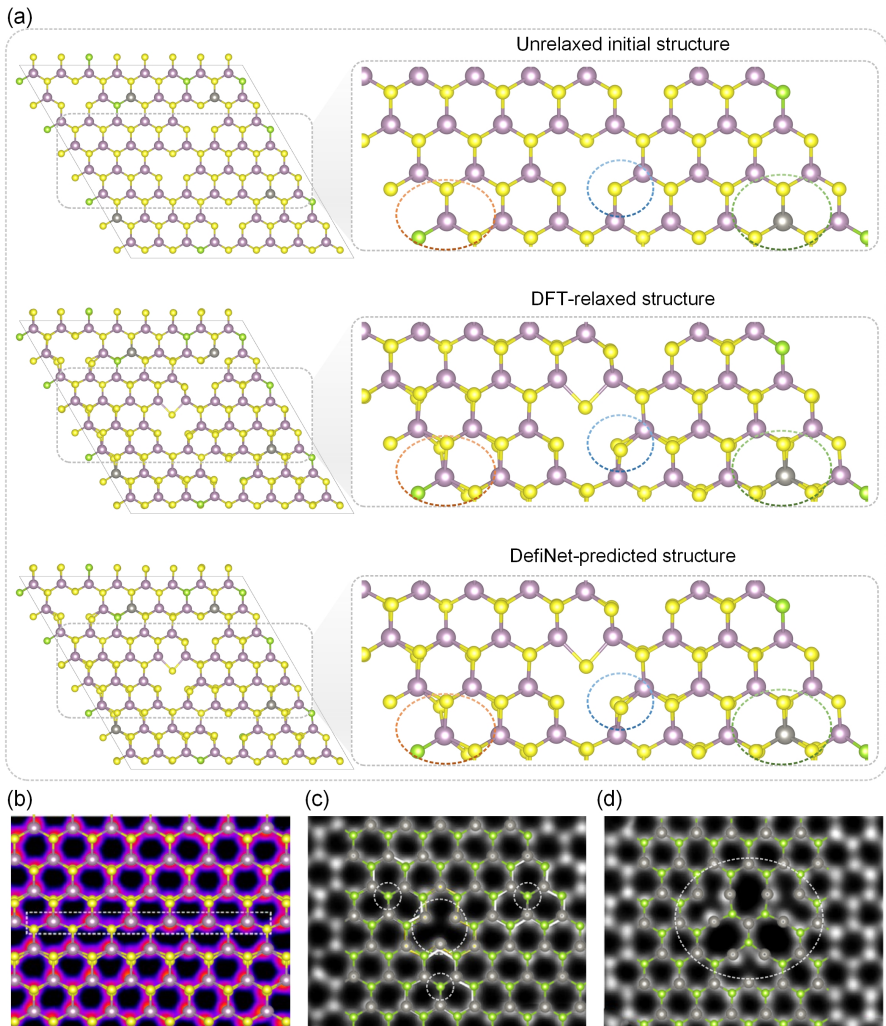
Fig. 6 Visualization of DefiNet-predicted defect structures and comparisons with STEM images. (a) Example of an MoS_2 crystal structure containing both substitutional and vacancy defects, alongside the corresponding DFT-relaxed and DefiNet-predicted structures. (b) STEM image of MoS_2 featuring a line defect, overlaid with the DefiNet-relaxed structure. Reprinted with permission from [42]. Copyright 2016 American Chemical Society. (c) STEM image of WSe_2 with mixed SV_{Se} and DV_{Se} defects, overlaid with the DefiNet-relaxed structure. (d) STEM image of WSe_2 with a three-fold symmetrical trefoil defect, overlaid with the DefiNet-relaxed structure. Defect sites are highlighted with white dotted lines for clarity.

3.9 Ablation study

To elucidate the contributions of DefiNet's key architectural components, we performed an ablation study focusing on its two main innovations:

- Universal Defect Representation with Defect-Aware Message Passing (DAMP): This component allows the model to capture complex interactions involving defects by representing all possible defect types within a unified graph framework.
- Defect-Aware Coordinate Updating (DACU): The RPV2ΔCoord and Vec2ΔCoord modules are designed to update atomic coordinates effectively, taking into account the unique influences of defects on the surrounding lattice.

We created two ablated versions of DefiNet to assess the impact of these components:

- Vanilla Model: This version removes both main components, DAMP and DACU.
- Vanilla + DAMP: This version includes the Universal Defect Representation with Defect-Aware Message Passing but removes the Defect-Aware Coordinate Updating modules.
- Vanilla + DAMP + DACU (DefiNet): This is the full DefiNet model incorporating both components.

The results on high-density datasets, as shown in Suppl. Fig. 6, indicate that both ablated models exhibit decreased performance compared to the full DefiNet. These findings confirm that both components are critical for DefiNet's superior performance. The Universal Defect Representation with DAMP ensures that all types of defects and their interactions are effectively modeled within a consistent framework. The DACU modules, including RPV2ΔCoord and Vec2ΔCoord, enable the model to predict atomic movements with high precision.

4 Discussion

Recently, GNNs have been used for defect property and structure analysis [12, 13, 44–49], showing great potential to reduce the high computational cost of DFT calculations. Two recent works [12, 13] have demonstrated that employing machine learning (ML) interatomic potentials can achieve both cost-effectiveness and accuracy in searching ground-state configurations of defect structures. However, these methods still rely on iterative processes, which may limit computational efficiency and scalability. In contrast, our proposed DefiNet explicitly considers complex defect-related interactions and fully eliminates the iterative process, leading to more accurate and rapid relaxation of defect crystal structures.

DefiNet's superior performance is attributed to its novel architecture that explicitly incorporates complex defect-related interactions through defect-aware message passing. By utilizing this novel strategy, DefiNet effectively captures interactions among vacancies, substitutions, and pristine atoms within a consistent graph framework. This approach addresses the limitations

of previous models that required reconstruction of defect-specific graphs and failed to consider vacancy interactions.

The model's ability to directly map initial structures to relaxed configurations eliminates the iterative process inherent in traditional relaxation methods. This not only enhances computational efficiency but also enables parallel computing capabilities, making DefiNet suitable for large-scale calculations. The incorporation of equivariance ensures that geometric transformations of the input structures are consistently reflected in the output, leading to more accurate predictions.

Compared to the previous state-of-the-art model, DeepRelax, DefiNet achieves substantial improvements in coordinate MAE. Additionally, DefiNet is approximately 26 times more computationally efficient than DeepRelax. These enhancements are significant, given that DeepRelax represents the leading method in single-step ML models for structural relaxation. Our scalability tests demonstrate that DefiNet maintains high accuracy when applied to larger systems beyond the sizes used during training. Moreover, our transferability tests show that DefiNet trained on high-density defect datasets generalizes well to low-density defect structures. These two properties significantly enhance the practicality of DefiNet.

The DFT validations confirm that the structures predicted by DefiNet are energetically favorable. Importantly, initiating DFT calculations from DefiNet-predicted structures significantly reduces the number of required ionic steps by approximately 87%, irrespective of defect complexity or system size. This hybrid approach leverages the speed of DefiNet and the precision of DFT, offering an efficient pathway for exploring defect structures in materials. While DefiNet demonstrates remarkable performance, certain limitations warrant discussion.

First, the current work is limited to 2D materials with point defects. Expanding DefiNet to handle 3D materials and more complex defect structures could significantly broaden its applicability.

Second, we assessed DefiNet's transferability by training the model on high-density defect data and testing it on low-density data, and vice versa, as detailed in Suppl. Note 6. The results indicate that DefiNet trained on high-density defects generalizes well to low-density scenarios, but training on low-density defects offers limited transferability to high-density cases. This suggests the importance of including a wide range of defect densities in the training data to maximize generalizability. Incorporating additional physical principles or constraints, such as electronic structure considerations, may further enhance the model's predictive capabilities.

Future work could focus on expanding the training datasets to include a broader spectrum of materials and defect types, as well as exploring the integration of DefiNet with other computational methods for multiscale modeling. Investigating the application of DefiNet to predict other properties influenced by defects, such as electronic or thermal properties, could also extend its utility in materials science.

In conclusion, DefiNet offers a powerful tool for the rapid relaxation of defect structures in crystalline materials. Its novel architecture addresses key challenges in modeling defect interactions and provides significant improvements over existing methods in both accuracy and efficiency. By facilitating large-scale and high-density defect analyses, DefiNet contributes to the advancement of materials science and the development of novel materials with enhanced functionalities.

Code availability

Data and code for DefiNet are available at https://github.com/Shen-Group/DefiNet.

Conflicts of interest

The authors declare that they have no competing interests.

Acknowledgements

References

[1] Davidsson, J., Bertoldo, F., Thygesen, K.S., Armiento, R.: Absorption versus adsorption: high-throughput computation of impurities in 2d materials. npj 2D Materials and Applications **7**(1), 26 (2023)

[2] Huang, P., Lukin, R., Faleev, M., Kazeev, N., Al-Maeeni, A.R., Andreeva, D.V., Ustyuzhanin, A., Tormasov, A., Castro Neto, A., Novoselov, K.S.: Unveiling the complex structure-property correlation of defects in 2d materials based on high throughput datasets. npj 2D Materials and Applications **7**(1), 6 (2023)

[3] Mosquera-Lois, I., Kavanagh, S.R., Walsh, A., Scanlon, D.O.: Identifying the ground state structures of point defects in solids. npj Computational Materials **9**(1), 25 (2023)

[4] Kazeev, N., Al-Maeeni, A.R., Romanov, I., Faleev, M., Lukin, R., Tormasov, A., Castro Neto, A., Novoselov, K.S., Huang, P., Ustyuzhanin, A.: Sparse representation for machine learning the properties of defects in 2d materials. npj Computational Materials **9**(1), 113 (2023)

[5] Thomas, J.C., Chen, W., Xiong, Y., Barker, B.A., Zhou, J., Chen, W., Rossi, A., Kelly, N., Yu, Z., Zhou, D., *et al.*: A substitutional quantum defect in ws2 discovered by high-throughput computational screening and fabricated by site-selective stm manipulation. Nature Communications **15**(1), 3556 (2024)

[6] Chen, C., Ong, S.P.: A universal graph deep learning interatomic potential for the periodic table. Nature Computational Science **2**(11), 718–728 (2022)

[7] Deng, B., Zhong, P., Jun, K., Riebesell, J., Han, K., Bartel, C.J., Ceder, G.: Chgnet as a pretrained universal neural network potential for charge-informed atomistic modelling. Nature Machine Intelligence, 1–11 (2023)

[8] Batzner, S., Musaelian, A., Sun, L., Geiger, M., Mailoa, J.P., Kornbluth, M., Molinari, N., Smidt, T.E., Kozinsky, B.: E (3)-equivariant graph neural networks for data-efficient and accurate interatomic potentials. Nature communications **13**(1), 2453 (2022)

[9] Batatia, I., Kovacs, D.P., Simm, G., Ortner, C., Csányi, G.: Mace: Higher order equivariant message passing neural networks for fast and accurate force fields. Advances in Neural Information Processing Systems **35**, 11423–11436 (2022)

[10] Park, Y., Kim, J., Hwang, S., Han, S.: Scalable parallel algorithm for graph neural network interatomic potentials in molecular dynamics simulations. Journal of Chemical Theory and Computation (2024)

[11] Ko, T.W., Ong, S.P.: Recent advances and outstanding challenges for machine learning interatomic potentials. Nature Computational Science **3**(12), 998–1000 (2023)

[12] Mosquera-Lois, I., Kavanagh, S.R., Ganose, A.M., Walsh, A.: Machine-learning structural reconstructions for accelerated point defect calculations. npj Computational Materials **10**(1), 121 (2024)

[13] Jiang, C., Marianetti, C.A., Khafizov, M., Hurley, D.H.: Machine learning potential assisted exploration of complex defect potential energy surfaces. npj Computational Materials **10**(1), 21 (2024)

[14] Schütt, K., Kindermans, P.-J., Sauceda Felix, H.E., Chmiela, S., Tkatchenko, A., Müller, K.-R.: Schnet: A continuous-filter convolutional neural network for modeling quantum interactions. Advances in neural information processing systems **30** (2017)

[15] Yang, Z., Wang, X., Dong, T., Li, Y., Lv, Q., Chen, C.Y.-C., Shen, L.: Lightweight equivariant interaction graph neural network for accurate

and efficient interatomic potential and force predictions. arXiv preprint arXiv:2311.02869 (2023)

[16] Kresse, G., Furthmüller, J.: Efficient iterative schemes for ab initio total-energy calculations using a plane-wave basis set. Physical review B **54**(16), 11169 (1996)

[17] Blöchl, P.E.: Projector augmented-wave method. Physical review B **50**(24), 17953 (1994)

[18] Xie, T., Grossman, J.C.: Crystal graph convolutional neural networks for an accurate and interpretable prediction of material properties. Physical review letters **120**(14), 145301 (2018)

[19] Musaelian, A., Batzner, S., Johansson, A., Sun, L., Owen, C.J., Kornbluth, M., Kozinsky, B.: Learning local equivariant representations for large-scale atomistic dynamics. Nature Communications **14**(1), 579 (2023)

[20] Pablo-García, S., Morandi, S., Vargas-Hernández, R.A., Jorner, K., Ivković, Ž., López, N., Aspuru-Guzik, A.: Fast evaluation of the adsorption energy of organic molecules on metals via graph neural networks. Nature Computational Science, 1–10 (2023)

[21] Li, H., Wang, Z., Zou, N., Ye, M., Xu, R., Gong, X., Duan, W., Xu, Y.: Deep-learning density functional theory hamiltonian for efficient ab initio electronic-structure calculation. Nature Computational Science **2**(6), 367–377 (2022)

[22] Gong, X., Li, H., Zou, N., Xu, R., Duan, W., Xu, Y.: General framework for e (3)-equivariant neural network representation of density functional theory hamiltonian. Nature Communications **14**(1), 2848 (2023)

[23] Zhong, Y., Yu, H., Su, M., Gong, X., Xiang, H.: Transferable equivariant graph neural networks for the hamiltonians of molecules and solids. npj Computational Materials **9**(1), 182 (2023)

[24] Zhong, Y., Yu, H., Yang, J., Guo, X., Xiang, H., Gong, X.: Universal machine learning kohn-sham hamiltonian for materials. Chinese Physics Letters (2024)

[25] Zhong, Y., Liu, S., Zhang, B., Tao, Z., Sun, Y., Chu, W., Gong, X.-G., Yang, J.-H., Xiang, H.: Accelerating the calculation of electron–phonon coupling strength with machine learning. Nature Computational Science, 1–11 (2024)

[26] Chen, C., Ye, W., Zuo, Y., Zheng, C., Ong, S.P.: Graph networks as a universal machine learning framework for molecules and crystals. Chemistry of Materials **31**(9), 3564–3572 (2019)

[27] Gasteiger, J., Groß, J., Günnemann, S.: Directional message passing for molecular graphs. In: International Conference on Learning Representations (ICLR) (2020)

[28] Choudhary, K., DeCost, B.: Atomistic line graph neural network for improved materials property predictions. npj Computational Materials **7**(1), 185 (2021)

[29] Unke, O.T., Chmiela, S., Gastegger, M., Schütt, K.T., Sauceda, H.E., Müller, K.-R.: Spookynet: Learning force fields with electronic degrees of freedom and nonlocal effects. Nature communications **12**(1), 7273 (2021)

[30] Unke, O.T., Meuwly, M.: Physnet: A neural network for predicting energies, forces, dipole moments, and partial charges. Journal of chemical theory and computation **15**(6), 3678–3693 (2019)

[31] Zhang, X., Zhou, J., Lu, J., Shen, L.: Interpretable learning of voltage for electrode design of multivalent metal-ion batteries. npj Computational Materials **8**(1), 175 (2022)

[32] Satorras, V.G., Hoogeboom, E., Welling, M.: E (n) equivariant graph neural networks. In: International Conference on Machine Learning, pp. 9323–9332 (2021). PMLR

[33] Omee, S.S., Louis, S.-Y., Fu, N., Wei, L., Dey, S., Dong, R., Li, Q., Hu, J.: Scalable deeper graph neural networks for high-performance materials property prediction. Patterns (2022)

[34] Schütt, K., Unke, O., Gastegger, M.: Equivariant message passing for the prediction of tensorial properties and molecular spectra. In: International Conference on Machine Learning, pp. 9377–9388 (2021). PMLR

[35] Haghighatlari, M., Li, J., Guan, X., Zhang, O., Das, A., Stein, C.J., Heidar-Zadeh, F., Liu, M., Head-Gordon, M., Bertels, L., *et al.*: Newtonnet: A newtonian message passing network for deep learning of interatomic potentials and forces. Digital Discovery **1**(3), 333–343 (2022)

[36] Han, J., Cen, J., Wu, L., Li, Z., Kong, X., Jiao, R., Yu, Z., Xu, T., Wu, F., Wang, Z., et al.: A survey of geometric graph neural networks: Data structures, models and applications. arXiv preprint arXiv:2403.00485 (2024)

[37] Prodan, E., Kohn, W.: Nearsightedness of electronic matter. Proceedings

of the National Academy of Sciences **102**(33), 11635–11638 (2005)

[38] Gilmer, J., Schoenholz, S.S., Riley, P.F., Vinyals, O., Dahl, G.E.: Neural message passing for quantum chemistry. In: International Conference on Machine Learning, pp. 1263–1272 (2017). PMLR

[39] Okabe, R., Chotrattanapituk, A., Boonkird, A., Andrejevic, N., Fu, X., Jaakkola, T.S., Song, Q., Nguyen, T., Drucker, N., Mu, S., et al.: Virtual node graph neural network for full phonon prediction. Nature Computational Science, 1–10 (2024)

[40] Deng, C., Litany, O., Duan, Y., Poulenard, A., Tagliasacchi, A., Guibas, L.J.: Vector neurons: A general framework for so (3)-equivariant networks. In: Proceedings of the IEEE/CVF International Conference on Computer Vision, pp. 12200–12209 (2021)

[41] Yang, Z., Zhao, Y.-M., Wang, X., Liu, X., Zhang, X., Li, Y., Lv, Q., Chen, C.Y.-C., Shen, L.: Scalable crystal structure relaxation using an iteration-free deep generative model with uncertainty quantification. Nature Communications **15**(1), 8148 (2024)

[42] Wang, S., Lee, G.-D., Lee, S., Yoon, E., Warner, J.H.: Detailed atomic reconstruction of extended line defects in monolayer mos2. ACS nano **10**(5), 5419–5430 (2016)

[43] Lin, Y.-C., Björkman, T., Komsa, H.-P., Teng, P.-Y., Yeh, C.-H., Huang, F.-S., Lin, K.-H., Jadczak, J., Huang, Y.-S., Chiu, P.-W., et al.: Three-fold rotational defects in two-dimensional transition metal dichalcogenides. Nature communications **6**(1), 6736 (2015)

[44] Witman, M.D., Goyal, A., Ogitsu, T., McDaniel, A.H., Lany, S.: Defect graph neural networks for materials discovery in high-temperature clean-energy applications. Nature Computational Science **3**(8), 675–686 (2023)

[45] Way, L., Spataru, C., Jones, R., Trinkle, D., Rowberg, A., Varley, J., Wexler, R., Smyth, C., Douglas, T., Bishop, S., et al.: Defect diffusion graph neural networks for materials discovery in high-temperature, clean energy applications (2024)

[46] Mannodi-Kanakkithodi, A., Xiang, X., Jacoby, L., Biegaj, R., Dunham, S.T., Gamelin, D.R., Chan, M.K.: Universal machine learning framework for defect predictions in zinc blende semiconductors. Patterns **3**(3) (2022)

[47] Frey, N.C., Akinwande, D., Jariwala, D., Shenoy, V.B.: Machine learning-enabled design of point defects in 2d materials for quantum and neuromorphic information processing. ACS nano **14**(10), 13406–13417 (2020)

[48] Rahman, M.H., Gollapalli, P., Manganaris, P., Yadav, S.K., Pilania, G., DeCost, B., Choudhary, K., Mannodi-Kanakkithodi, A.: Accelerating defect predictions in semiconductors using graph neural networks. APL Machine Learning **2**(1) (2024)

[49] Fang, Z., Yan, Q.: Leveraging persistent homology features for accurate defect formation energy predictions via graph neural networks. arXiv preprint arXiv:2407.05204 (2024)